CrossMark

Photoluminescence properties of hexagonal indium tin oxide nanopowders prepared by solvothermal method

Fei Liang, Jia-Xiang Liu* ⓘ

Abstract Hexagonal structure indium tin oxide (ITO) nanopowders were prepared by a solvothermal process at only 175 °C for 24 h and post-annealing at 400 °C, using metal indium and $SnCl_4 \cdot 5H_2O$ as the raw materials. The morphology, crystal structures and structure defects of products were, respectively, analyzed by scanning electron microscopy (SEM), X-ray diffraction (XRD) and confocal microprobe Raman system, the elemental state was investigated by X-ray photoelectron spectroscopy (XPS), and the optical properties were carried out by ultraviolet–visible (UV-Vis) and photoluminescence (PL) spectrophotometers. The results show that the products are hexagonal structure with a particles size of 28–41 nm; the morphology of products consists of sphere and irregular cubic. When pH values of solution increase, the content of oxygen vacancies increases and the optical band gap varies from 3.59 to 3.78 eV. The products exhibit strong emission at 417 nm with an excitation of 370 nm, and the PL intensity of samples increases with pH values increasing. Contrasting to cubic structure ITO powder, the hexagonal structure ITO has narrower optical band gap and higher PL intensity under the same excitation wavelength.

Keywords Hexagonal indium tin oxide; Solvothermal; Oxygen vacancies; Optical band gap; Photoluminescence

F. Liang, J.-X. Liu*
The State Key Laboratory of Chemical Resource Engineering,
The Beijing Key Laboratory of Electrochemical Process and
Technology for Materials, College of Materials Science and
Engineering, Beijing University of Chemical Technology,
Beijing 100029, China
e-mail: ljxpost@263.net

1 Introduction

The Sn-doped In_2O_3 n-type semiconductor oxides, generally called ITO (indium tin oxide), are widely used in flat panel displays, fuel-sensitized solar cell and gas sensor due to its low resistance and excellent optical properties [1, 2]. There are two different crystal structures of In_2O_3: the cubic structure (c-In_2O_3) and the hexagonal structure (h-In_2O_3). The corresponding crystal structures of ITO are cubic structures (c-ITO) and hexagonal structures (h-ITO). The h-ITO or h-In_2O_3 has shown many special properties such as high lithium storage capacity for lithium-ion batteries [3], high gas sensitivity [4] and high photocatalytic activity [5].

However, the preparation of h-ITO is more difficult than that of c-ITO because the hexagonal structures are generally achieved at a high temperature or high pressures [6]. For example, Liu et al. [7] obtained h-In_2O_3 at room temperature, but above 15.3 GPa, Kim et al. [8] just obtained the mixed powders of h-ITO and c-ITO using co-precipitation. Yu et al. [9] synthesized h-In_2O_3 fibers by pyrolysing InOOH at 490 °C. Solvothermal method is an effective way to synthesize high-purity, high-crystallinity and well-dispersed h-ITO powders due to high reaction activity and simple device. Recently, many studies have been reported for synthesis of h-ITO with solvothermal method [10–12]. However, to obtain the well-dispersed and high-crystallinity h-ITO under mild conditions, the reaction conditions in solvothermal process such as types of solvent, pH, reaction temperature and time are still necessary to be studied deeply.

The properties of photoluminescence (PL) are important part of semiconductor light emission research fields. It has been reported that the bulk In_2O_3 materials show no PL emission at room temperature [13]. However, owing to the

oxygen defects forming in the preparation process and quantum confinement effect, ITO nanostructures exhibit PL phenomenon. Previous works generated great interest in the relationship between PL intensity and SnO_2 content in ITO specimen [14] and the PL properties of different morphologies [15, 16]. However, the study on the emission mechanism of ITO and the influence of fabrication conditions on PL intensity were rarely reported. Besides, it has been known that pH values have a significant influence on the crystal growth rate and the structure of growth units which determine the morphology and the content of crystal defects [17]. However, controlling oxygen vacancy concentrations by changing pH values in solvothermal method and its effect on PL properties has seldom been reported.

In this work, the well-dispersed and high-crystallinity h-ITO powders were synthesized by solvothermal method with binary solvents methanol–ethylene glycol, and the effect of pH values on the content of oxygen vacancies and PL properties were discussed.

2 Experimental

$In(NO_3)_3$ was prepared by vigorous stirring indium (11.4 g) with concentrated nitric acid (HNO_3) at 50 °C, then mixed with $SnCl_4 \cdot 5H_2O$ (3.56 g) at In_2O_3 to SnO_2 weight ratio of 90:10. 100 milliliters above-mixed solution were divided into five portions, and ammonia was added into the above-mixed solution to keep certain pH values, such as 3.5, 5.5, 7.5 and 9.5, then the amount of methanol and ethylene glycol (the ratio of volume = 1:2) as solvent was added with 20 vol% of the mixed solution. After stirred for 1 h, the suspensions were transferred into Teflon-lined stainless steel autoclaves and heated at 175 °C for 24 h, then naturally cooled to room temperature. The mixtures were washed with water and ethanol and then centrifuged until there are no chlorine and nitrate ions, and dried at 80 °C for 10 h. The precursors were finally heated at 400 °C for 3 h to produce Sample 1. Sample 2 was prepared by adding ammonia into the rest of mixed solution to pH 9.5, and then, the precursor was washed and dried just like above mentioned. Finally, it was calcined at 400 °C for 3 h directly.

The crystal structures were examined by powder X-ray diffractometer (XRD, D8 Advance). Structural defects were characterized by confocal microprobe Raman system (Renishaw InVia) with the excitation wavelength of 514.5 nm. Morphologies of the products were investigated by scanning electron microscope (SEM, HITACHI S-4700), and the distribution histogram of particle size was obtained by the statistic of 50 particles in each SEM image. The carrier concentrations of products were obtained from Hall effect measurement system (Phystech, RH2030).

Diffusion reflection spectra were obtained from ultraviolet–visible spectrophotometer (UV–Vis, UV-3600). X-ray photoelectron spectroscopy (XPS, ESCALAB 250, Mg K radiation) was employed to investigate elemental state. Photoluminescence (PL) properties of product were carried on F-7000 fluorescence spectrophotometer. Absolute quantum yields (QY) were recorded on a FLS980 steady-state spectrometer (Edinburgh Instruments, England).

3 Results and discussion

3.1 Phase analysis

Figure 1 shows XRD patterns of products prepared under different conditions, and it can be seen that diffraction peaks of Sample 2 can be indexed to the cubic structure In_2O_3 (JCPDS No. 06-0416). However, all diffraction peaks of Sample 1 (pH = 3.5–9.5) can be indexed to the hexagonal structure In_2O_3 (JCPDS No. 22-336). No peaks from other crystalline phases are found. The Raman spectra were recorded to confirm crystalline structures and investigate structural defects (Fig. 2). On the basis of group theory analysis, the hexagonal structure In_2O_3 belongs to the space group of $R\bar{3}c$, D_{3d}^6, and the optical modes (Γ_{opt}) in the crystal can be expressed by the following equation: [18]

$$\Gamma_{opt} = 2A_{1g} + 5E_g + 2A_{1u} + 2A_{2u} + 3A_{2g} + 4E_u \quad (1)$$

where the vibrations with symmetries A_{1u}, A_{2u}, A_{2g} and E_u are infrared-active or Raman-active, the vibrational with symmetries A_{1g} and E_g is Raman-active, the Raman shifts at 163 and 504 cm^{-1} are corresponding to the vibration mode of A_{1g}, while Raman shifts at 219, 386 and 590 cm^{-1} are assigned to E_g, which agree well with the reported values of h-In_2O_3 in Ref. [19]. The Raman shifts at 504 cm^{-1} are assigned to the stretching vibration of In–O–In. Moreover, it also reflects the oxygen vacancies in h-In_2O_3 structure [20]. It can be seen that the relative
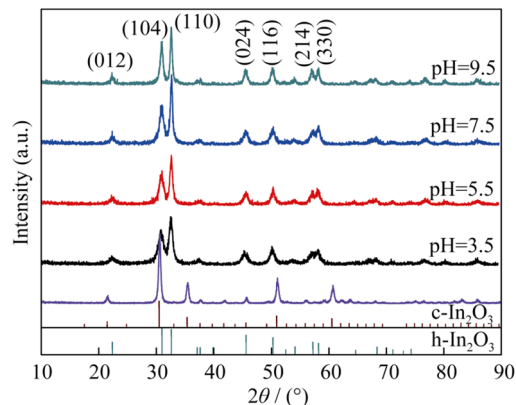

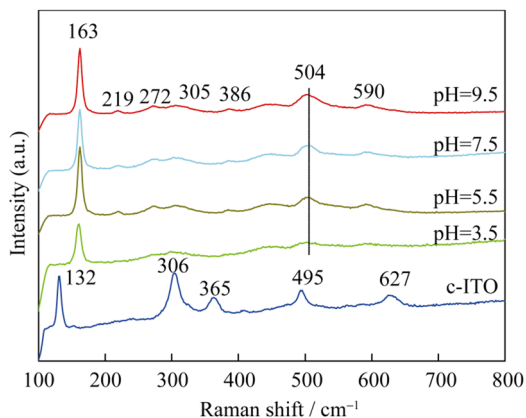**Fig. 1** XRD patterns of as-prepared ITO samples

Fig. 2 Raman spectra of as-prepared ITO samples

intensity of 504 cm^{-1} gradually increases with the increase in pH values, indicating that there are more oxygen vacancies at high pH values. When OH$^-$ concentration increases, the octahedron of InO$_6$ is strongly distorted [21]. This process leads to that the breakage of In–O bond becomes easier, and then, more oxygen vacancies are formed. The c-In$_2$O$_3$ belongs to the space group of $Ia3$, T_h^7. The optical modes in the crystal can be expressed by the following equation: [18]

$$\Gamma_{opt} = 4A_g + 4E_g + 14T_g + 5A_u + 5E_u + 16T_u \qquad (2)$$

where the vibrations with symmetries A_g, E_g and T_g are Raman-active, the vibrations with symmetry A_u and E_u are non-active, and T_u is infrared-active. As shown in Fig. 2, c-ITO Raman vibrational modes locate at about 132, 306, 365, 495 and 627 cm^{-1}, Raman spectrum of Sample 2 is in

good agreement with the reported values of c-In$_2$O$_3$ in Ref. [22]. The Raman spectra of h-ITO and c-ITO are similar with the corresponding Raman spectra of h-In$_2$O$_3$ and c-In$_2$O$_3$ because the main contribution to the vibrational modes comes from the host lattice of h-In$_2$O$_3$ and c-In$_2$O$_3$.

3.2 Morphology analysis

Figure 3 shows SEM images and particle size distribution histogram of ITO prepared at different conditions. It can be seen from SEM images that the morphology of c-ITO is sphere with an average particle size of 39 nm. The morphologies of h-ITO vary with the solution pH values. The majority of morphologies are irregular cubic structure, and the rest are spheres with an average particle size of 33 nm (pH = 3.5). When the pH values of solution increase to 5.5, the amount of sphere structures slightly increases and the average particle size is 41 nm. However, the morphologies mostly present as spheres with an average particle size of 38 nm when solution pH value is 7.5. Finally, the majority of morphologies become irregularly cubic with an average particle size of 28 nm (pH = 9.5). SEM analysis indicates that two kinds of morphologies, irregularly cubic and spherical, are observed at different solution pH values. The amount of spheres increases firstly and then reduces with pH values increasing.

3.3 PL property analysis

Figure 4 shows diffuse reflection spectra of ITO prepared at different conditions, and the absorption spectra of
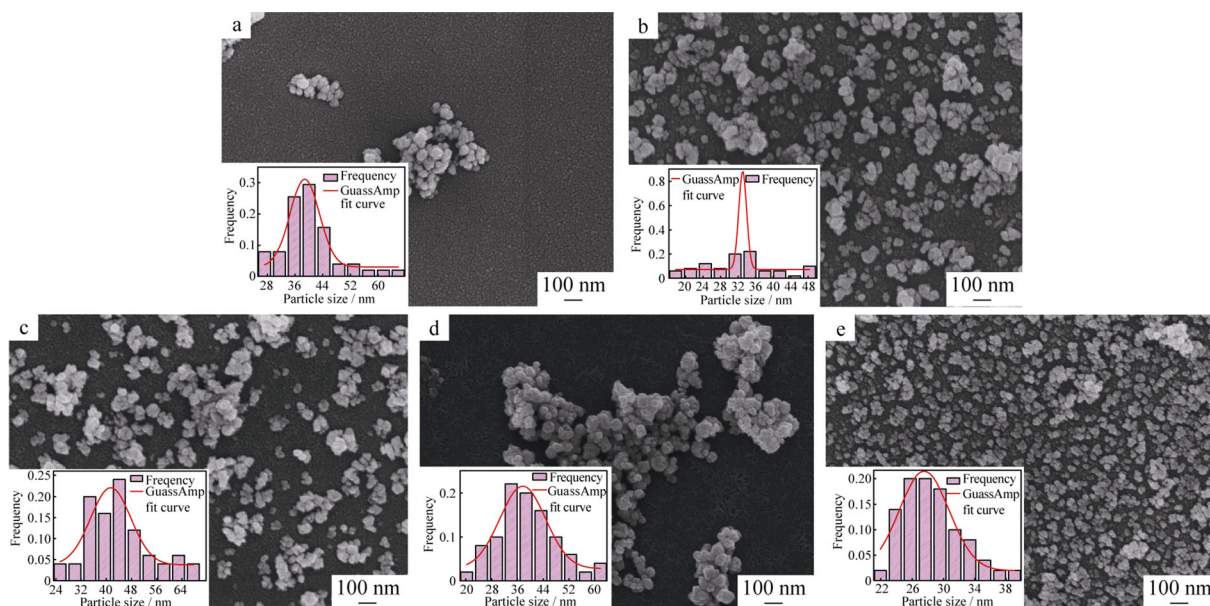

Fig. 3 SEM images and inset histograms of size distribution of particles of ITO samples prepared at different conditions: **a** c-ITO, **b** pH = 3.5, **c** pH = 5.5, **d** pH = 7.5 and **e** pH = 9.5

Fig. 4 Diffusion reflection spectra of as-prepared ITO samples
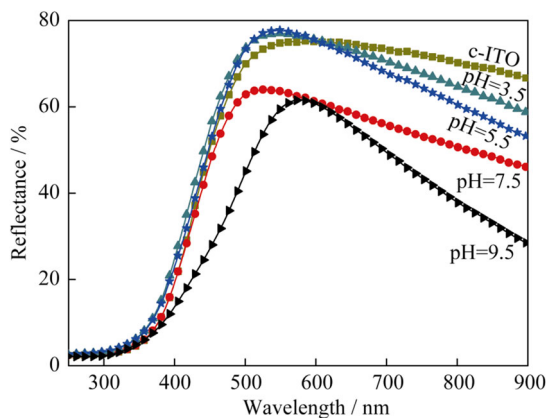

Fig. 6 Plot of $(\alpha h v)^2$ as function of $h v$ for as-prepared ITO samples
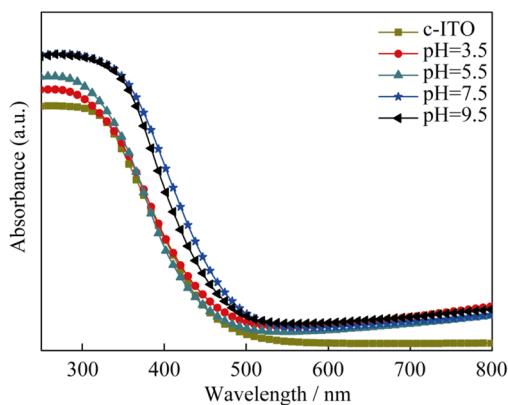

Fig. 5 UV–Vis absorption spectra of as-prepared ITO samples

products can been converted by the Kubelka–Munk (KM) theory using the following equation: [23]

$$\frac{(1 - R_\infty)^2}{2R_\infty} = \frac{K}{S} = F(R) \tag{3}$$

where K is the absorption coefficient, S is the scattering coefficient, R_∞ is the reflectance of the sample with infinite thickness, and $F(R)$ is the KM function. Figure 5 shows UV–Vis absorption spectra converted by diffuse reflection spectra. It can be seen that the ITO samples show strong absorption at 240–450 nm. Moreover, the optical band gap can be estimated by the following equation: [24]

$$(\alpha h v)^2 = A(h v - E_g) \tag{4}$$

where A is a constants related to the valence and conduction band of material, $h v$ is photon energy, α is the absorption coefficient, and E_g is the optical band gap. The optical band gap can be obtained by linearly fitting on the edge of the corresponding curve. As shown in Fig. 6, the E_g values of as-prepared ITO samples are 3.59 eV (pH = 3.5), 3.68 eV (pH = 5.5), 3.74 eV (pH = 7.5), 3.78 eV (pH = 9.5) and 3.82 eV (c-ITO), respectively. It
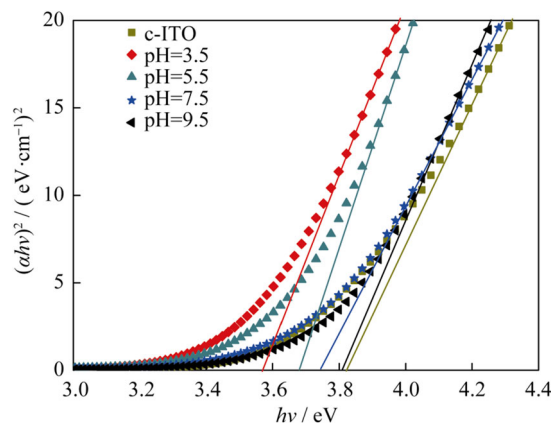
is clear that the E_g values of c-ITO are higher than that of h-ITO due to the difference of energy band structure between h-In$_2$O$_3$ and c-In$_2$O$_3$. It has been know that the valence band of h-In$_2$O$_3$ and c-In$_2$O$_3$ consists of O 2p and In 4d; however, the bottom of conduction band of c-In$_2$O$_3$ is made up of O 2p and In 5s, and the bottom of conduction band h-In$_2$O$_3$ is made up of In 5s [25]. Moreover, the E_g values of h-ITO are higher than the intrinsic band gap of 3.5 eV and increase with pH values increasing. The concentration of oxygen vacancies increases with solution pH values increasing which has been discussed at Raman spectra. Furthermore, it has been known that one oxygen vacancy can provide conduction band with two free electrons after ionizing process, leading to the increase in carrier concentrations. Therefore, the increase in E_g value can be explained by Burstein–Moss effect. On the basis of this model, the electrons of valence band excited to conduction band need more energy. It can be explained by that donor electrons occupy the bottom of the conduction band when carrier concentrations increase, which makes E_g values increase. The relationship between carrier concentrations (n) and optical band gap (E_g) is expressed by the following equation [26]

$$E_g - E_0 = \frac{(\pi h)^2}{2m_r^*} \left(\frac{3n}{\pi}\right)^{2/3} \tag{5}$$

where E_0 is the intrinsic band gap, m_r^* is the reduced effective mass, and h is Planck constant. Figure 7 shows the variation of E_g with $n^{2/3}$. There is a good correlation between optical band gap and $n^{2/3}$, which was confirmed by Gupta et al. [27]. The results indicate that the increase in E_g is induced by the increase in carrier concentrations, consistent with above discussions. To verify the existence of oxygen vacancies, the chemical and structural evolutions of h-ITO nanopowders were analyzed by XPS. Figure 8 shows O 1s XPS spectra of ITO samples prepared at different pH values. Three peaks, including 529.9, 531.1 and
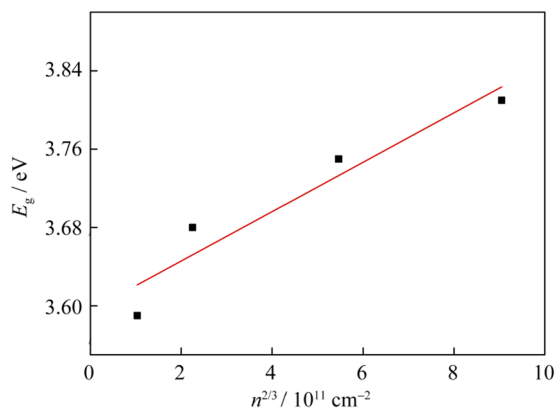
Fig. 7 Plot of band gap (E_g) as a function of $n^{2/3}$ of h-ITO prepared at different pH values

Fig. 9 PL spectra of as-prepared ITO samples

531.7 eV, are found in all the h-ITO nanopowders. The peaks at 529.9 and 531.7 eV can be assigned to oxygen in h-In_2O_3 lattices without and with oxygen vacancies, respectively [28]. Besides, the peak at 531.1 eV can be assigned to oxygen in SnO_2 lattices. The analysis on content of oxide lattice with oxygen vacancies was performed based on an area integration of each O 1s peak (Fig. 8e). It is observed that the content of oxygen in h-In_2O_3 lattices with oxygen vacancies increases when pH values increases. These results imply that the increase in carrier concentration may be due to the increase in oxygen vacancies.

Figure 9 shows the room temperature PL spectra of as-prepared ITO samples at different conditions. The PL
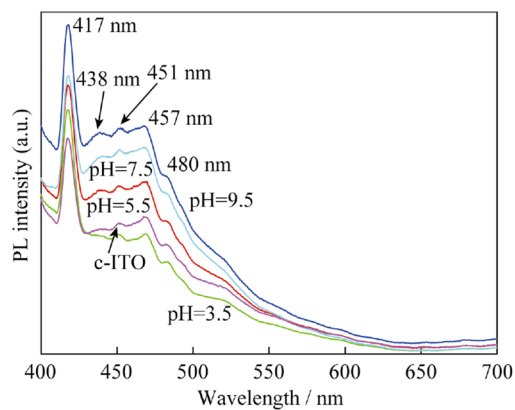
spectra of as-prepared ITO samples are similar with 370-nm excitation, and five peaks of 417, 438, 451, 457 and 480 nm are observed in blue light region. The PL intensity of h-ITO is higher than that of c-ITO and increases with pH values increasing. Since the energy of emission peaks (417 nm at 2.98 eV, 438 nm at 2.84 eV, 451 nm at 2.75 eV, 451 nm at 2.72 eV and 480 nm at 2.59 eV) are lower than the band gap of h-ITO (3.59–3.78 eV), the visible emission cannot be assigned to the direct recombination of a conduction electron in In 5s band and a hole in O 2p valence band. Furthermore, the possibility of the observed PL arising from a quantum confinement effect also can be excluded, because the diameters of the present h-ITO nanopowders seem too large to show a quantum
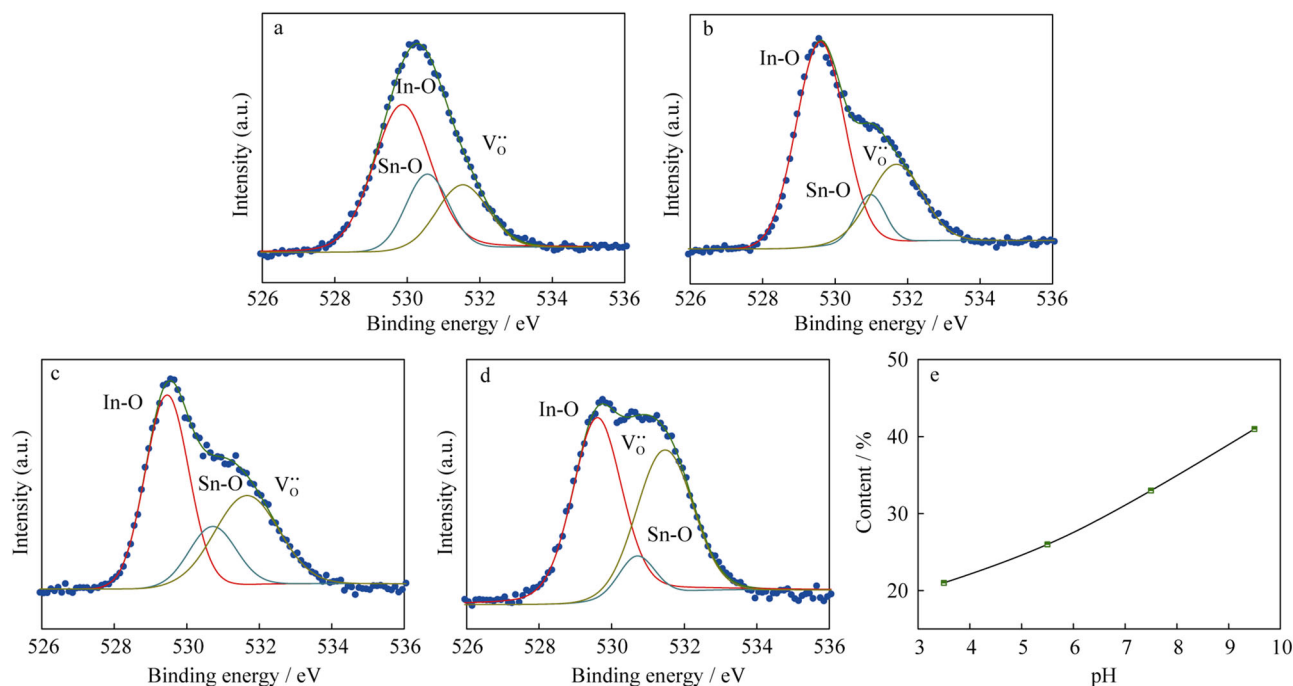

Fig. 8 O 1s XPS spectra of h-ITO nanopowders prepared at different pH values: **a** pH = 3.5, **b** pH = 5.5, **c** pH = 7.5 and **d** pH = 9.5; **e** content of oxide lattice with oxygen vacancies as a function of pH value
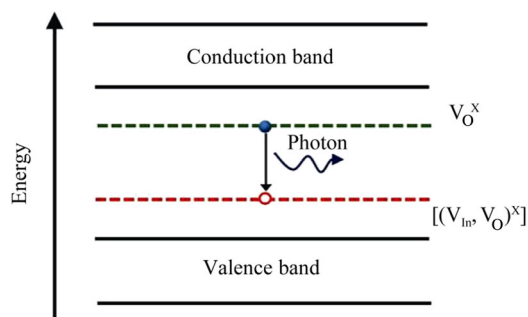
Fig. 10 Mechanism diagram of luminescence process

Fig. 11 Quantum yield of h-ITO nanopowders prepared at different pH values

confinement effect (the critical Bohr radius of In_2O_3 is about 2.14 nm) [29]. Therefore, the intensive blue light emission can be attributed to oxygen vacancies (V_O^X) and indium oxygen vacancy centers [$(V_{In}, V_O)^X$]. The $(V_{In}, V_O)^X$ may be acted as the acceptors and V_O^X as the donors. After excitation of the acceptor, a hole on the acceptor and an electron on a donor are created according to the following formula [30]:

$$V_O^{\cdot} + (V_{In}, V_O)^{/} + hv \rightarrow (V_{In}, V_O)^X + (V_O)^X \tag{6}$$
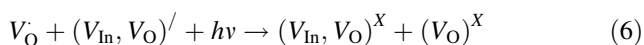
There are two steps in the luminescence process. Firstly, an electron in donor level (V_O^X) may be captured by a hole on an acceptor [$(V_{In}, V_O)^X$] to form a trapped exciton. In the next step, the trapped exciton recombines radiatively to emit blue light. Thus, the blue emission occurs via the reverse process, which is illustrated in Fig. 10. The mechanism of blue light emission of ITO is similar with that of In_2O_3. However, the donor level of ITO consists of oxygen vacancies (V_O^X) and defects of In substituted Sn (Sn_{In}). Consequently, the luminescence process of ITO also includes another process in which Sn_{In} is the donor level when the excitons have radiative recombination. This process of radiative recombination of excitons can be expressed by the following formula:

$$Sn_{In}^{\cdot} + (V_{In}, V_O)^{/} + hv \rightarrow (V_{In}, V_O)^X + Sn_{In}^X \tag{7}$$
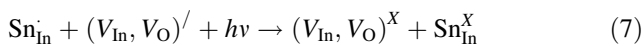
The specific process is like process in Eq. (6). The effects of process in Eq. (7) on the luminous intensity of all of products are nearly identical under the same doping concentrations of SnO_2. Therefore, it can be inferred from the process in Eq. (6) that the number of excitons, created by the hole on acceptor capturing electrons, increases and the probability of radiative recombination of excitons increases. As results, the number of emitted photons increases when the oxygen vacancy concentrations increase. To confirm the influence of content of oxygen vacancies on PL intensity, the absolute quantum yields (QY) of h-ITO nanopowders obtained at different pH values are shown Fig. 11. The quantum yield (QY) of
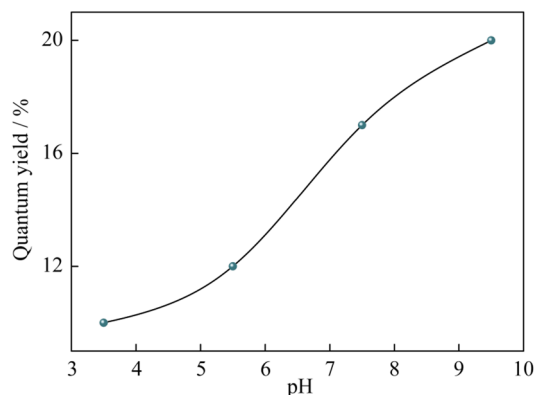
h-ITO nanopowders increases when pH values range from 3.5 to 9.5. It indicates that luminescent ability increases with the content of oxygen vacancies increasing.

4 Conclusion

The h-ITO powders were synthesized by solvothermal method with binary solvent methanol–ethylene glycol, and the influence of content of oxygen vacancies on PL properties was discussed. It is observed that the content of oxygen vacancies, carrier concentrations and PL intensity of h-ITO strongly depend on pH values. When pH values increase, the optical band gap of h-ITO increases from 3.59 to 3.78 eV and carrier concentrations of h-ITO range from 3.32×10^{16} to 9.07×10^{17} cm^{-3}. Moreover, the results of PL spectra present that crystal structure has significant effects on PL intensity, but has little influence on peaks. Additionally, PL intensity of h-ITO nanopowders is determined by the content of oxygen vacancies when doping concentrations of SnO_2 are identical, and PL intensity increases with the content of oxygen vacancies increasing. In contrast to c-ITO, the h-ITO shows higher PL intensity. It indicates that h-ITO nanopowders may have great potential application in light-emitting devices.

References

[1] Neri G, Bonavita A, Micali G, Rizzo G, Pinna N, Niederberger M, Ba J. A study on the microstructure and gas sensing properties of ITO nanocrystals. Thin Solid Films. 2007;515(24): 8637.
[2] Peng LP, He AL, Fang L, Yang XF. Structure and properties of indium-doped ZnO films prepared by RF magnetron sputtering under different pressures. Rare Met. 2015;1(34):1.

[3] Liu D, Lei WW, Qin S, Hou LT, Liu ZW, Cui QL, Chen Y. Large-scale synthesis of hexagonal corundum-type In$_2$O$_3$ by ball milling with enhanced lithium storage capabilities. J Mater Chem A. 2013;1(17):5274.

[4] Song P, Han D, Zhang HH, Li J, Yang ZX, Wang Q. Hydrothermal synthesis of porous In$_2$O$_3$ nanospheres with superior ethanol sensing properties. Sens Actuators, B. 2014;196:434.

[5] Chen LY, Wang ZX, Zhang ZD. Corundum-type tubular and rod-like In$_2$O$_3$ nanocrystals: synthesis from designed InOOH and application in photocatalysis. New J Chem. 2009;33(5):1109.

[6] Solieman A, Zayed MK, Alamri SN, Al-Dahoudi N, Aegerter MA. Corundum nanostructure ITO film fabrication: an approach for physical properties assessment. Mater Chem Phys. 2012;134(1):127.

[7] Liu D, Lei WW, Zou B, Yu SD, Hao J, Wang K, Liu BB, Cui QL, Zou GT. High-pressure X-ray diffraction and Raman spectra study of indium oxide. J Appl Phys. 2008;104(8):083506.

[8] Kim B, Kim SM, Lee JH, Kim JJ. Effect of phase transformation on the densification of coprecipitated nanocrystalline indium tin oxide powders. J Am Ceram Soc. 2002;85(8):2083.

[9] Yu DB, Yu SH, Zhang SY, Zuo J, Wang D, Qian YT. Metastable hexagonal In$_2$O$_3$ nanofibers templated from InOOH nanofibers under ambient pressure. Adv Funct Mater. 2003;13(6):497.

[10] Yin JF, Cao HQ. Synthesis and photocatalytic activity of single-crystalline hollow rh-In$_2$O$_3$ nanocrystals. Inorg Chem. 2012;51(12):6529.

[11] Chen C, Chen D, Jiao XL, Wang CQ. Ultrathin corundum-type In$_2$O$_3$ nanotubes derived from orthorhombic InOOH: synthesis and formation mechanism. Chem Commun. 2006;44:4632.

[12] Farvid SS, Radovanovic PV. Phase transformation of colloidal In$_2$O$_3$ nanocrystals driven by the interface nucleation mechanism: a kinetic study. J Am Chem Soc. 2012;134(16):7015.

[13] Yang HX, Liu L, Liang H. Phase-controlled synthesis of monodispersed porous In$_2$O$_3$ nanospheres via an organic acid-assisted hydrothermal process. Cryst Eng Comm. 2011;13(15):5011.

[14] Sun ZY, He JB, Kumbhar A, Fang JY. Nonaqueous synthesis and photoluminescence of ITO nanoparticles. Langmuir. 2010;26(6):4246.

[15] Wang GX, Park J, Wexler D, Park MS, Ahn JH. Synthesis, characterization, and optical properties of In$_2$O$_3$ semiconductor nanowires. Inorg Chem. 2007;46(12):4778.

[16] Ho CH, Chan CH, Tien LC, Huang YS. Direct optical observation of band-edge excitons, band gap, and fermi level in degenerate semiconducting oxide nanowires In$_2$O$_3$. J Phys Chem C. 2011;115(50):25088.

[17] Wahab R, Kim YS, Shin HS. Synthesis, characterization and effect of Ph variation on zinc oxide nanostructures. Mater Trans. 2009;50(8):2092.

[18] Wang CY, Dai Y, Pezoldt J, Lu B, Kups T, Cimalla V, Ambache O. Phase stabilization and phonon properties of single crystalline rhombohedral indium oxide. Cryst Growth Des. 2008;8(4):1257.

[19] Wu MM, Wang C, Zhao Y, Xiao LS, Zhang C, Yu XP, Luo BF, Hu B, Fan WP, Shi WD. Hydrothermal synthesis of porous rh-In$_2$O$_3$ nanostructures with visible-light-driven photocatalytic degradation of tetracycline. Cryst Eng Comm. 2015;17(11):2336.

[20] Gan JY, Lu XH, Wu JH, Xie SL, Zhai T, Yu MH, Zhang ZS, Mao YC, Wang SCI, Shen Y, Tong YX. Oxygen vacancies promoting photoelectrochemical performance of In$_2$O$_3$ nanocubes. Sci Rep. 2013;3:1021.

[21] Buchholz DB, Ma Q, Alducin D, Ponce A, Jose-Yacaman M, Khanal R, Medvedeva JE, Chang RPH. The structure and properties of amorphous indium oxide. Chem Mater. 2014;26(18):5401.

[22] Hafeezullah, Yamani ZH, Iqbal J, Qurashib A, Hakeem A. Rapid sonochemical synthesis of In$_2$O$_3$ nanoparticles their doping optical, electrical and hydrogen gas sensing properties. J Alloys Compd. 2014;616:76.

[23] Jeevanandam P, Mulukutla RS, Phillips MS, Chaudhuri S, Erickson LE, Klabunde KJ. Near infrared reflectance properties of metal oxide nanoparticles. J Phys Chem C. 2007;111(5):1912.

[24] Tao BL, Zhang Y, Han DZ, Li YP, Yan ZF. Synthesis of corundum-type In$_2$O$_3$ porous spheres and their photocatalytic properties. J Mater Chem A. 2014;2(15):5455.

[25] Walsh A, Silva D, Wei SH, Körber C, Klein A, Piper LF, DeMasi A, Smith KE, Panaccione G, Torelli P, Payne DJ, Bourlange A, Egdell RG. Nature of the band gap of In$_2$O$_3$ revealed by first-principles calculations and X-ray spectroscopy. Phys Rev Lett. 2008;100(16):167402.

[26] Qu F, Zhang T, Gu HW, Qiu QQ, Ding FZ, Peng XY, Wang HY. Electrical and optical properties of ZnO: Al films with different hydrogen contents in sputtering gas. Rare Met. 2015;34(3):173.

[27] Gupta RK, Ghosh K, Patel R, Kaho PK. Effect of substrate temperature on opto-electrical properties of Nb-doped In$_2$O$_3$ thin films. J Cryst Growth. 2008;310(19):4336.

[28] Choi CH, Han SY, Su YW, Fang Z, Lin LY, Cheng CC, Chang CH. Fabrication of high-performance, low-temperature solution processed amorphous indium oxide thin-film transistors using a volatile nitrate precursor. J Mater Chem C. 2015;3(4):854.

[29] Zeng FH, Zhang X, Wang J, Wang LS, Zhang LN. Large-scale growth of In$_2$O$_3$ nanowires and their optical properties. Nanotechnology. 2004;15(5):596.

[30] Wu XC, Hong JM, Han ZJ, Tao YR. Fabrication and photoluminescence characteristics of single crystalline In$_2$O$_3$ nanowires. Chem Phys Lett. 2003;373(12):28.